The International Journal of Advanced Manufacturing Technology (2024) 130:4919–4931
https://doi.org/10.1007/s00170-024-12967-4

ORIGINAL ARTICLE

Effect of stress relief and solubilization heat treatments on laser additive manufactured Inconel 625: microstructure and properties

Douglas Bon[1] · Thiago Cavalcante[1] · Anselmo Thiesen[2] · Henrique Santos[2] · Jhonattan Gutjahr[2] · Osvaldo Cintho[3] · Reginaldo Coelho[1] · Marcelo Falcão de Oliveira[1] · Giovani Gonçalves Ribamar[4] · Julian Arnaldo Avila[5,6]

Received: 23 August 2023 / Accepted: 2 January 2024 / Published online: 19 January 2024
© The Author(s) 2024

Abstract
This work assesses the effect of the energy input and the stress relief and solubilization heat treatment on the microstructure and mechanical properties of an Inconel 625 alloy processed by laser additive manufacturing using directed energy deposition. Two processing conditions were used to deliver high productivity with a high energy input (HEI) and another with better geometrical precision using a lower energy input (LEI). The mechanical test samples were built vertically and horizontally aligned with the tensile test direction. The samples were submitted to residual stress relief (SR) and SR + solubilization (S) heat treatments (SR + S). Results showed increased elongation with solubilization heat treatment, while UTS and YS decreased with heat treatment combination, which was linked to the stronger texture developed in HEI condition. Samples built in the vertical direction presented lower YS. The fracture toughness of solubilization heat-treated samples showed higher values, while LEI gave just slightly higher values. Although the microstructural and mechanical features are similar between the HEI and LEI conditions, the first stands out because parts can be fabricated quickly without losing mechanical performance under quasi-static conditions, impact fracture tests, or the production of unwanted phases.

Keywords Inconel 625 · Laser-directed energy deposition · Additive manufacturing · Mechanical properties · Heat treatments · Stress relief · Solubilization

1 Introduction

Regarding metallic alloys with aerospace applications, two methods are highlighted within the available laser additive manufacturing (LAM): (i) laser-directed energy deposition (LDED) and (ii) laser powder bed fusion (LPBF). LDED delivers a higher deposition rate than LPBF [1], yet LPBF provides better-quality surfaces and can make intricate components [2]. The most important LDED parameters are the laser beam diameter, heat source power, transverse speed, mass flow rate, hatch spacing, layer thickness, and overlayer percentage. Other indirect variables, such as energy input [3] and interaction time [1], are useful to check the impact of heating on the microstructure. LDED offers the possibility of building large components with dimensions around 1000 mm^2 with changing diameters, thin walls, and some step (30°) building angles, which is useful for complex geometries such as nozzles [4]. Additionally, the degrees of freedom, building volume capacity, building orientation, and the type of powder used might affect the final quality of the built components.

✉ Julian Arnaldo Avila
julian.arnaldo.avila@upc.edu

1 Materials Engineering Deparment, University of São Paulo (USP), São Carlos, SP 13563-120, Brazil

2 SENAI Innovation Institute for Manufacturing Systems and Laser, Joinville, SC 89218-153, Brazil

3 State University of Ponta Grossa (UEPG), Ponta Grossa, PR 84030-900, Brazil

4 Department of Metallurgical and Materials Engineering, University of São Paulo (USP), São Paulo, SP 05508-010, Brazil

5 Research Group in Structures and Mechanics of Materials (REMM), Department of Strength of Materials and Structural Engineering, Universitat Politècnica de Catalunya (UPC), Barcelona 08028, Spain

6 School of Engineering, São Paulo State University (UNESP), São João da Boa Vista, SP 13876-750, Brazil

Despite the importance of the nickel-base Inconel 625 (IN625), which has applications in different industries, such as aerospace, marine, chemical, and petrochemical [5], few studies can be found addressing the correlation between microstructural features after additive manufacturing and post-heating treatments and mechanical properties. Fullen et al. [6] processed an Inconel 625 from four vendors by LPBF. They found that the weight percentage of N affected the microstructure and mechanical behavior after solution treatment at 1100 °C for 3 h. Nguejio et al. [7] processed the Inconel 625 by LPBD and LDED and compared the mechanical behavior of horizontal samples after heat treatments. They found that the additive manufactured samples presented higher yield strength (YS) in the as-built condition in comparison to wrought samples (482 MPa); however, the ultimate tensile strength (UTS), 955 MPa at the wrought material, was 25 MPa lower at the LPBF and 120 MPa higher at the LDED. After the heat treatments at 900 °C for 1 h and 1100 °C for 1 h, the UTS followed a trend of higher values at the LDED samples. However, their elongation to fracture was always below the LPBF. Regarding the orientation fabrication, typically, the horizontal samples present a better ultimate tensile strength than vertical samples but lower elongation to fracture, whose behavior is justified due to the load application direction, parallel to the layers' depositions in the horizontal and perpendicular in the vertical directions. According to Hu et al. [8], the main reason for the anisotropy of YS is the difference in grain boundary strengthening effect and the distribution of the leaves phase; however, the crystallographic texture component of the as-built IN625 specimens corresponding to < 100 > can also affect the anisotropic behavior in additive manufactured Inconel 625 [9].

All metallic components incorporate residual stresses (RS) during the transformation processes or even during the smooth machining finishing. Several LAM processing parameters affect residual stresses' magnitude, such as temperature gradient, cool-down phase, solid-state phase transformations, and internal stress imbalance [10]. RS can limit the quality of LAM components, affecting mechanical properties, dimensional stability, and reliability. Therefore, some strategies can be adopted to reduce RS in LAM parts, such as preheating, hybrid processing, and post-heat treatments [10]. As recommended for nozzles produced by LDED, making several parts above 1100 mm in diameter and 1200 mm in height for rocket engines, it is necessary to apply stress relief in the built part and building plate before removing the part from the platform [4]. According to heat treatments suggested for wrought IN625, the RS relief heat treatment should be conducted at 870 °C for 1 h [11]. However, Stoudt et al. [12], using isothermal heat treatments between 650 and 1050 °C at different times to evaluate the delta phase (δ) evolution, found a complete displacement to shorter times of the time–temperature-transformation curve for the δ development in LAM products. Therefore, the conventional recommendation at 870 °C is not an option for LAM parts since a larger presence of δ can compromise ductility and fracture toughness [13]. Based on these results, to reduce the residual stresses and avoid the δ formation, the best stress relief route would be 800 °C for 1 h or longer [12].

Regarding the dissolution of the δ phase, it is known that a solution heat treatment above 1100 °C will remove this phase in conventional wrought Inconel 625 [13]. According to the Heat Treater's Guide [11], a heat treatment at 1150 °C for 2 h with rapid cooling until 540 °C would prevent the precipitation of δ-phase in intermediate temperatures. Fullen et al. [14] compared the microstructural and mechanical properties of four different chemical compositions of the IN625 alloy while also applying four other heat treatments (SR, i.e., 900 °C for 1 h, SR + solubilization at 1100 °C, SR + solubilization at 1120 °C, and SR + solubilization at 1150 °C). They noticed differences in the effects of the heat treatments on the different chemical compositions, where nitrogen was the element with the highest influence. They also reported that RS led to the hardest condition, while the solution treatments allowed recrystallization, thus softening the matrix, also observed by Farias et al. [15]. Marchese et al. [5], using LPBF, reported similar results in terms of mechanical properties using solution treatments at 1080 °C for 1 h and 1150 °C for 1 h. Finally, Nguejio et al. [6] compared two heat treatments using 900 °C for 1 h and 1100 °C for 1 h in an LDED and LPBF-manufactured Inconel 625. They reported that for both fabrication processes treated at 1100 °C for 1 h, the suppression of the columnar dendrites improved the ductility. Additionally, hot isostatic pressing delivers equiaxed microstructure, but the grains can coarsen; however, the mechanical strength decreases [9].

Despite the rising number of scientific publications and projects related to LAM, there is a considerable lack of information about the processing parameters of LDED, microstructure evolution, and mechanical properties after the post-heat treatments of the Inconel 625. Therefore, this work aims to study the effect of stress relief and solubilization heat treatments in the IN625 processed by LDED. Two processing conditions were employed, one with a high energy input (HEI) and another with a low energy input (LEI) but focused on the layers' resolution. Due to the differences in the processing parameters and the material's property anisotropy (observed in either the scan or the build direction, i.e., horizontal and vertical direction), the influence of the heat treatments was analyzed using tensile and impact tests. In addition, a complete microstructural analysis was correlated with the mechanical properties.

2 Experimental procedure

2.1 Sample production

A laser-based directed energy deposition machine processed Inconel 625 alloy powder. The powder particle size distribution ranged between 53–63 µm (25%), 64–105 µm (47%), and 106–125 µm (28%). Its chemical composition, characterized by optical emission spectroscopy, is shown in Table 1, which agrees with the ASTM F3056 standard for the AM IN625 alloy [16].

Figure 1 shows the LDED equipment used and the samples fabricated in this study. The parts were produced in an RPM Innovations 535 machine, a deposition system with an installed 1070 nm wavelength 3000 W laser source from IPG Photonics YLS-3000-CT. A linear scan strategy with 45° rotation between layers was used and maintained constant for all fabrication conditions. As shown in Fig. 1, horizontal and vertical rectangular components were fabricated to further machine the tensile and Charpy samples. Two platforms were produced. A total of four samples for tensile tests, four samples for impact

Table 1 Chemical composition of the IN625 powder in wt%

	Ni	Cr	Mo	Si	Fe	Mn	Nb	C
Measured	Bal	20.80	8.90	0.43	0.51	0.37	3.51	0.01
ASTM F3056 [16]	Bal	20.0—23.0	8.0—10.0	Max. 0.5	Max. 5.0	Max. 0.5	3.15—4.15	Max. 0.01

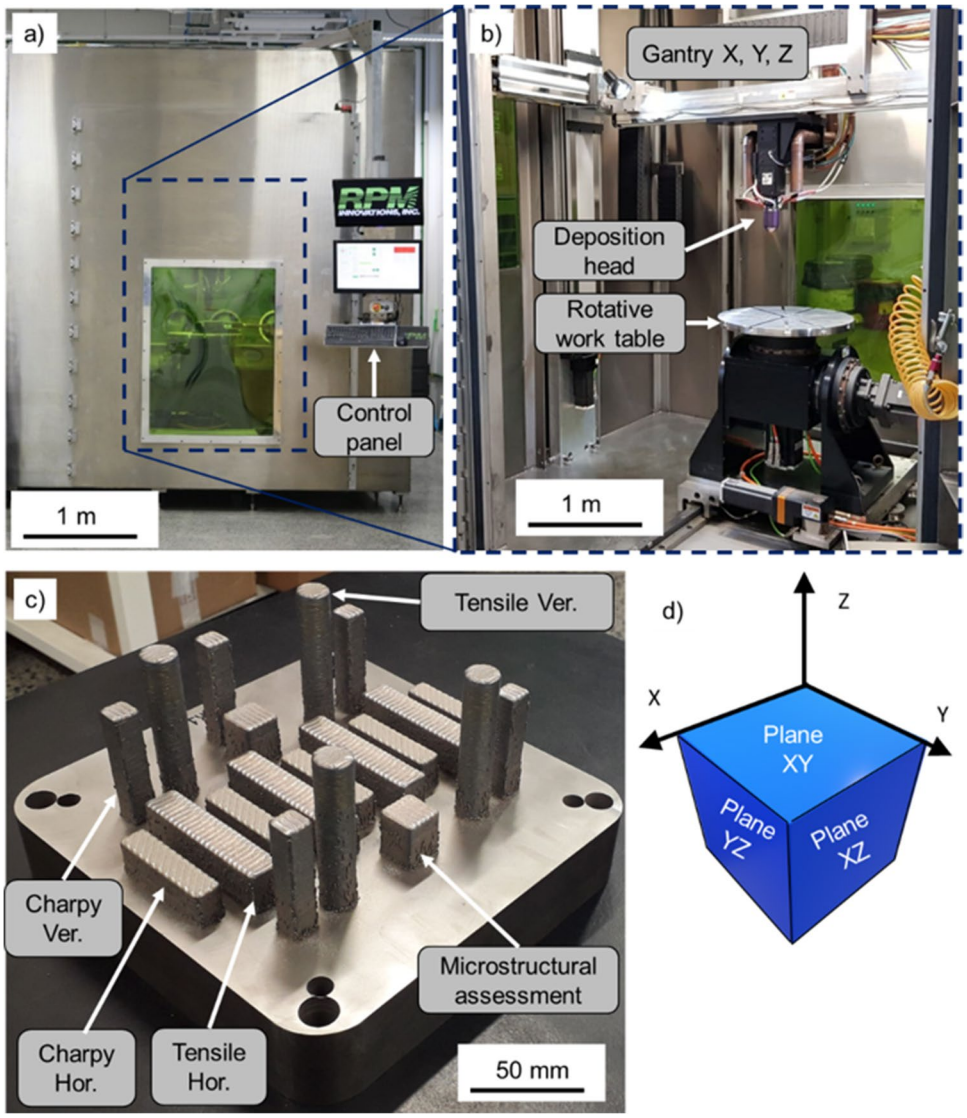

Fig. 1 LDED machine and samples produced by RPM Innovation, INC., showing **a** general view of the equipment, **b** a zoom-in view of the deposition system, **c** the sample distribution in the platform after fabrication, and **d** axis fabrication

tests, and two square blocks of 15 mm for microstructural assessment were processed in each working platform. All samples to analyze were taken far from the bottom to avoid chemical segregation, which would lead to a gradient of properties.

Two different processing conditions were chosen based on previous tests following an in-house parametrization procedure [17], namely, (i) high energy input (HEI) and (ii) low energy input (LEI) conditions. The values were calculated using the energy input equation, $EI = P/(v \cdot g)$, at [3]. Table 2 depicts the parameters used. The computed energy input (EI), considering the transverse speed (v) and mass flow rate (g), presents a strong contrast between both conditions, being 234 and 111 J s mm^{-1} g^{-1} for HEI and LEI conditions, respectively. In the LEI condition, a layer with a height of ≈ 0.65 mm was deposited. In comparison, the HEI condition had a size of ≈ 1 mm, corresponding to the interaction time between the laser and the material ($t_i = d/v$) [1]. The higher the time, the higher the deposition rate. Thus, small laser diameters result in higher process resolution, and high laser dimeters enhance productivity, which has been proven for PBF technology [1] but also applies to LDED.

2.2 Heat cycles

Based on the literature shown in the introduction, to reduce the residual stresses and avoid the δ formation, the best stress relief route would be 800 °C for 1 h [7]. After the stress relief, our main objective was to remove the presence of deleterious phases and to avoid grain growth at high temperatures and treatment times. Therefore, the most representative solution treatment for different additive manufacturing processes seems to be 1100 °C for 1 h [5, 6, 8, 9]. Hence, two heat treatments were chosen: one aiming for stress relief at 800 °C for 1 h – (SR), and the other has a combined effect of stress relief followed by a solubilization (S) at 1100 °C for 1 h – (SR + S). We must highlight our purpose in recreating large parts (> 1000 mm^3) scenarios. Therefore, an industrial furnace was used to conduct the heat treatments. Thus, the measured heating and cooling rates were ≈ 4.3 °C·min^{-1} and ≈ 0.65 °C·min^{-1}. In total, eight conditions were studied: two deposition heat inputs, two building directions, and two heat treatments, besides the as-built samples used in the microstructural comparisons. CALPHAD equilibrium calculations were carried out using the Thermocalc® software and the TCNI9 database for equilibrium phase determination, composition, and volume fraction.

Table 2 LDED process parameters for HEI and LEI conditions of the IN625 alloy

		Condition	
		HEI	LEI
d — laser beam diameter (mm)		1.78	0.76
P — heat source power (J/s)		1237.00	1174.00
v transverse speed (mm/s)		12.70	25.40
g — mass flow rate (g/s)		0.42	0.42
Hatch spacing (mm)		1.67	1.38
EI — energy input (J·s/mm·g) [3]		234	111
t_i — interaction time (s) [1]		0.140	0.030
Layer thickness (mm)		1.02	0.65
Overlayer	(%)	20	20
	(mm)	0.82	0.52
Efficiency (%)		37.40	31.20

2.3 Mechanical properties and microstructural characterization

An Instron 5988 universal machine with 400 kN load capacity and an advanced video extensometer were used for tensile tests. The tests followed the ASTM E8 standard [18]. The samples with threaded ends (M14), a reduced section of Ø 9 mm with a length of 45 mm, and a gauge length of 36 mm were used to conduct the tensile test at a crosshead rate of 1.3 mm min^{-1}. The Charpy tests followed the ASTM E23 standard [19] in a 390 J pendulum impact tester, Instron S1-1D3, using type A Charpy V-notched samples (55 × 10 × 10 mm^3). All mechanical tests were conducted at room temperature.

Samples were prepared for microstructural analysis by standard metallography followed by etching by immersion for 3–30 min in a solution comprised of 15 ml of HCl + 10 ml of acetic acid + 10 ml of HNO_3 [20]. The microstructural features were assessed with a laser confocal microscope Olympus 3D laser LEXT 4100 and a scanning electron microscope FEI INSPECT F-50. Electron backscatter diffraction measurements were conducted using an Oxford detector in a TESCAN-FEG MIRA 3 scanning electron microscope after samples were ground and polished with diamond suspension and colloidal silica. The operation voltage and step size were 15 keV and 1.6–2.4 µm, respectively. EBSD data were processed using the free, open-source package MTEX. X-ray diffractograms were acquired using an MDR-XLX'Pert-PRO X-ray diffractometer equipped with Mo-Kα radiation, with a wavelength of 0.71 Å.

Quantitative stereology was used to quantify the porosity in the as-built conditions. The metallographic samples without etching were used to extract seven photos from different positions of the samples with an approximated area of 262 × 197 µm. Then, the defect size was obtained by analyzing images using the ImageJ software [10, 11].

3 Results

3.1 Macrostructural and microstructural features

Table 3 shows the equilibrium phase volume fraction calculated at 800 °C and 1100 °C, temperatures for SR and S heat treatment, respectively. The temperature usually chosen for stress relief heat treatment (800 °C) presents high amounts of Ni_3Nb and σ phases, where those phases show high amounts of Mo, Cr, Nb, and Ni. It is worth mentioning that the σ phase was labeled by the Thermocalc software, presenting a stoichiometry of CrNiMo at 800 °C, similar to the Laves phase mentioned by some references [15, 21, 22].

The micrographs in Fig. 2 depict the as-built (first column), SR heat-treated (second column), and SR + S heat-treated (third column) samples microstructure. The first row refers to the HEI condition, while the second one refers to the LEI condition. In Fig. 2a and d, it can be observed the differences between the depth and width of the melting pool between the deposition conditions, where the HEI condition presented depths around 1134 ± 35 µm, while the LEI condition showed values around 609 ± 25 µm. Besides these differences, the microstructure is composed mainly of columnar grains, which start in one melt pool and wrought to the next on some occasions.

Table 3 Phase volume percentage calculated under equilibrium using CALPHAD method by Thermocalc® software and TCNI9 database

Temperature (°C)	Phase volume percentage			
	γ-Ni	NbC	Ni_3Nb	σ
800	84.19	0.08	6.54	9.19
1100	99.99	0.01	-	-

Microstructural analysis, at first look, showed some minor differences between HEI and LEI conditions in higher magnification micrographs (Fig. 3). However, more significant differences can be noticed when comparing SR and SR + S heat treatments. SR + S samples presented a finer structure and generally smaller dendrite spacing when compared to SR samples. The density analyses conducted by quantitative stereology theory showed that the HEI depicted 99.9% and the LEI 99.6%. Therefore, a slightly higher porosity was found in the LEI condition. Common gas porous were found in both conditions, and the LEI also showed a lack of fusion defects.

Figure 4 shows the crystallographic orientation map results for as-built and heat-treated samples. The first observation is that the columnar structure did not disappear even after solubilization heat treatment (S), which could not be observed on the optical micrographs, as depicted in

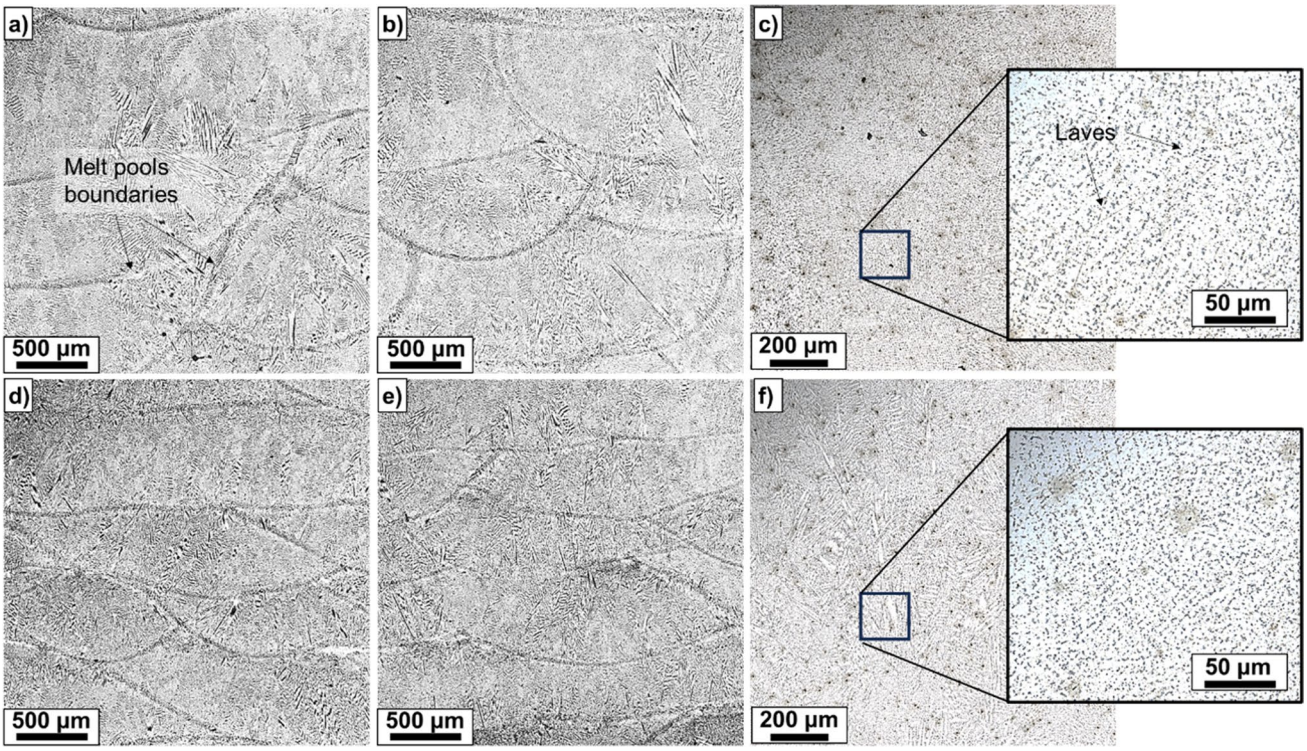

Fig. 2 Micro-scale features of the deposited layers in the *XZ* plane of the as-built (first column), SR − heat-treated (second column), and SR + S heat-treated samples (third column). The first row refers to the HEI condition, while the second row refers to the LEI condition

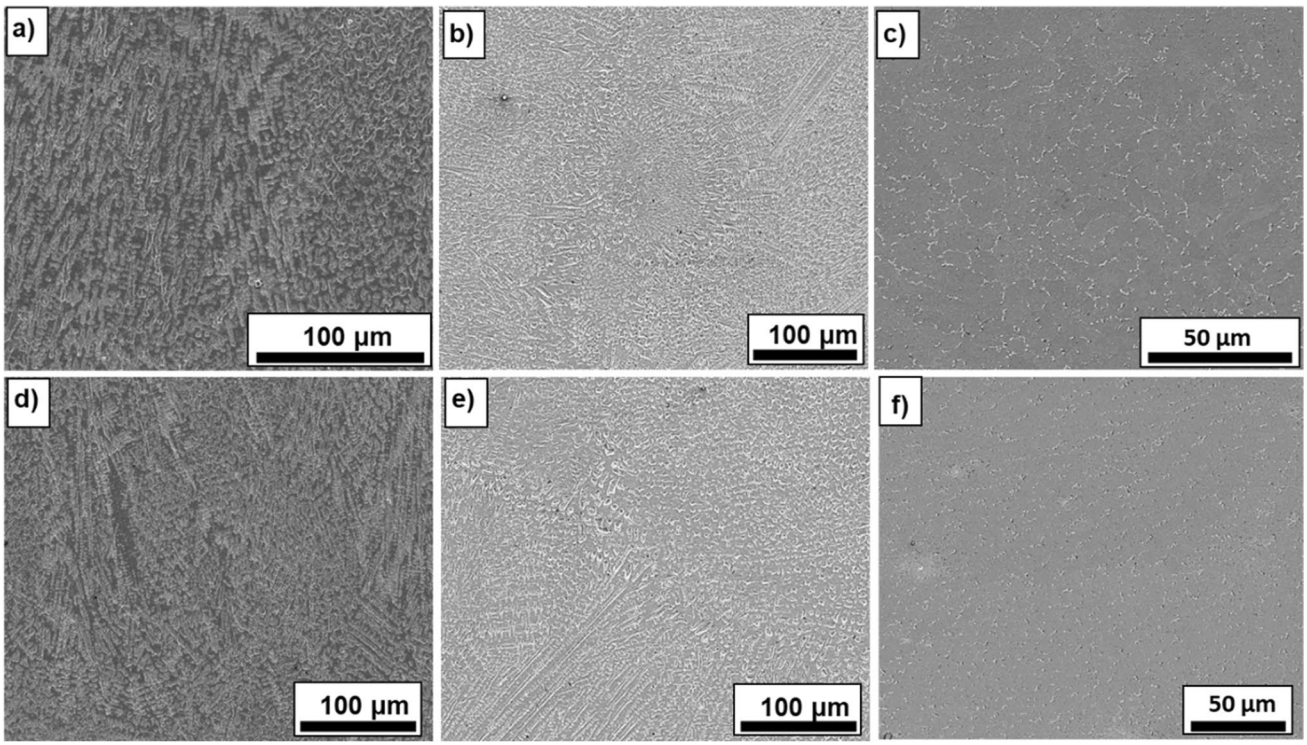

Fig. 3 Microstructural features of HEI in the upper row and LEI in the lower row. The first column shows the as-built condition (**a** and **d**), the second column the stress relief state (**b** and **e**), and the third column the stress relief + solubilization conditions (**c** and **f**). The magnification of the images was chosen to depict the microstructural details better

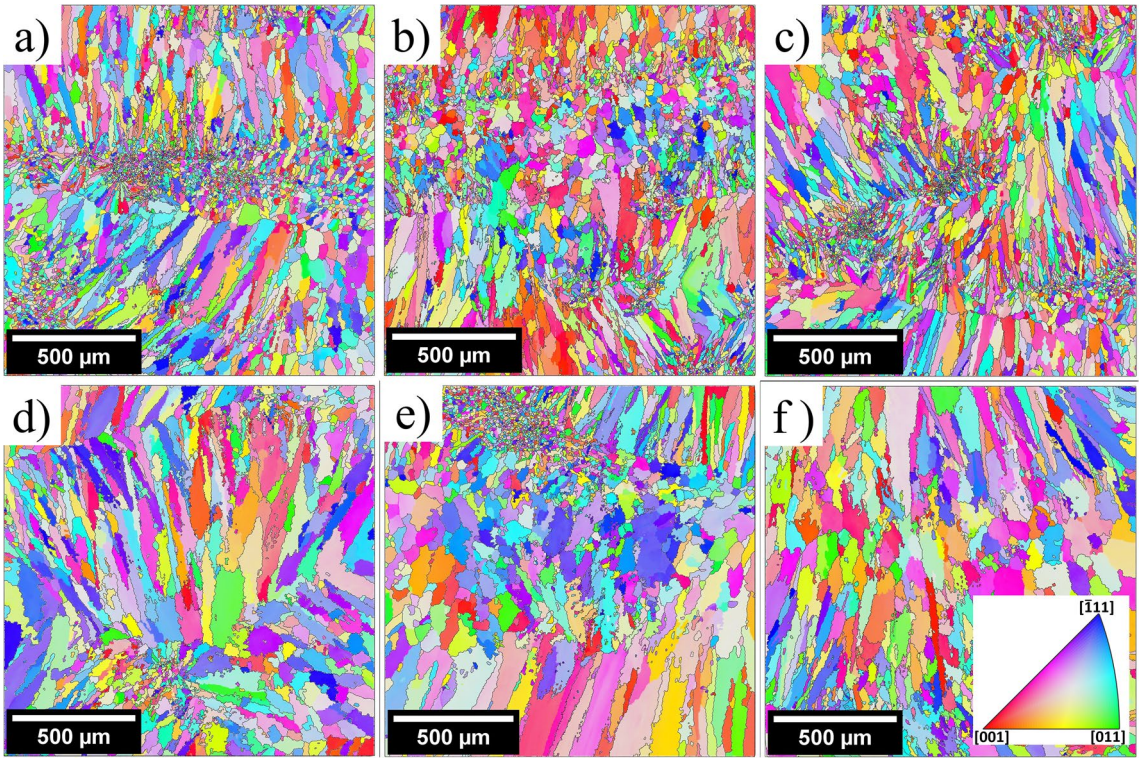

Fig. 4 EBSD orientation map for LEI (first row) and HEI (second row) conditions, showing **a**, **d** as built, **b**, **e** after stress relief heat treatment, and **c**, **f** after the combination of stress relief and solubilization heat treatment. Figure f displays a color key for crystallographic orientation related to cubic symmetry. High angle grain boundaries (> 15°) are displayed as solid black lines

Fig. 2c–d. However, it can be observed recrystallized regions mainly between beads. This feature was also reported in this type of material in previous work [14] and using the same alloy processed by LPBF [23], which depicts complete recrystallization after solution treatment at 1100 ºC for 3 h. The HEI samples also present visible coarser equiaxed and columnar grains than LEI samples. However, no other big difference can be observed between the heat treatments [24].

Orientation distribution functions (ODF) are shown in Fig. 5 and were calculated concerning the *y* direction and weighted by the grain area. All ODFs were plotted in the same intensity range, varying from 1 (random orientation) to 8. The maximum intensity calculated from each condition is shown in the upper left side of each subfigure. There is no significant crystallographic microtexture regarding the LEI condition, achieving a maximum intensity of 3.1 for the LEI – SR + S condition. For the latter, a $\{1\bar{1}3\}$ ∥ BD weak texture can be seen. On the other side, there are stronger textures developed for the as-built HEI sample, showing $\{322\}<236>$∥ BD texture, which evolves to cube texture ($\{001\}<0\bar{1}0>$∥ BD) with solubilization heat treatment.

Figure 6a shows the X-ray diffractograms of the as-built and heat-treated conditions in the LEI and HEI modes. As a result, only the typical peaks of the γ-Ni phase were observed in all conditions [25]. Figure 6b shows the γ-Ni lattice parameter. Both as-built conditions present similar lattice parameter values. However, it decreases with SR heat treatment for HEI conditions, while the opposite is observed for the other. With further solubilization, the lattice parameter for the LEI condition decreases, while for the HEI, it stands constant. Figure 6c shows the hardness value obtained from as-built and heat-treated samples. While LEI hardness seems to reduce with the combination of the heat treatments, the HEI condition does not. The hardness of the HEI – SR + S is lower than the others.

3.2 Tensile results

Figure 7 shows the tensile test results for heat-treated samples with built direction aligned to *Z* direction (vertical — Ver) and building direction aligned to *X* direction (horizontal — Hor). Figure 7a presents the engineering stress–strain curves for each condition in the vertical and horizontal building direction and processing conditions. The summary of the quantitative mechanical properties, i.e., yield strength (YS), ultimate tensile strength (UTS), and elongation to fracture (ELF), is shown in Fig. 7b–d. YS decreases with solubilization heat treatments for both LEI and HEI conditions. Additionally, YS is lower on the

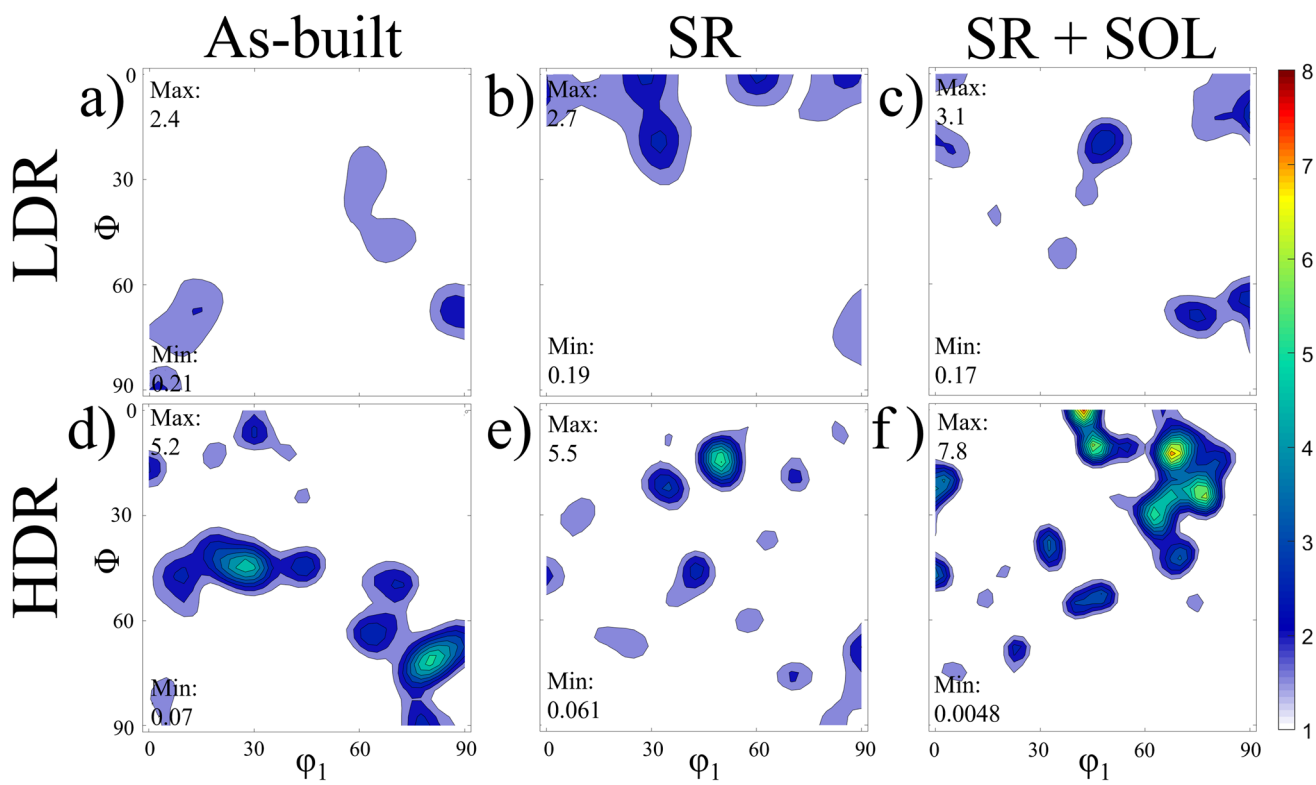

Fig. 5 Orientation distribution function (ODF) at φ2 = 45° for as-built and heat-treated samples. All the ODFs were normalized with the same intensity range, showing the maximum intensity in the upper left side of each subfigure

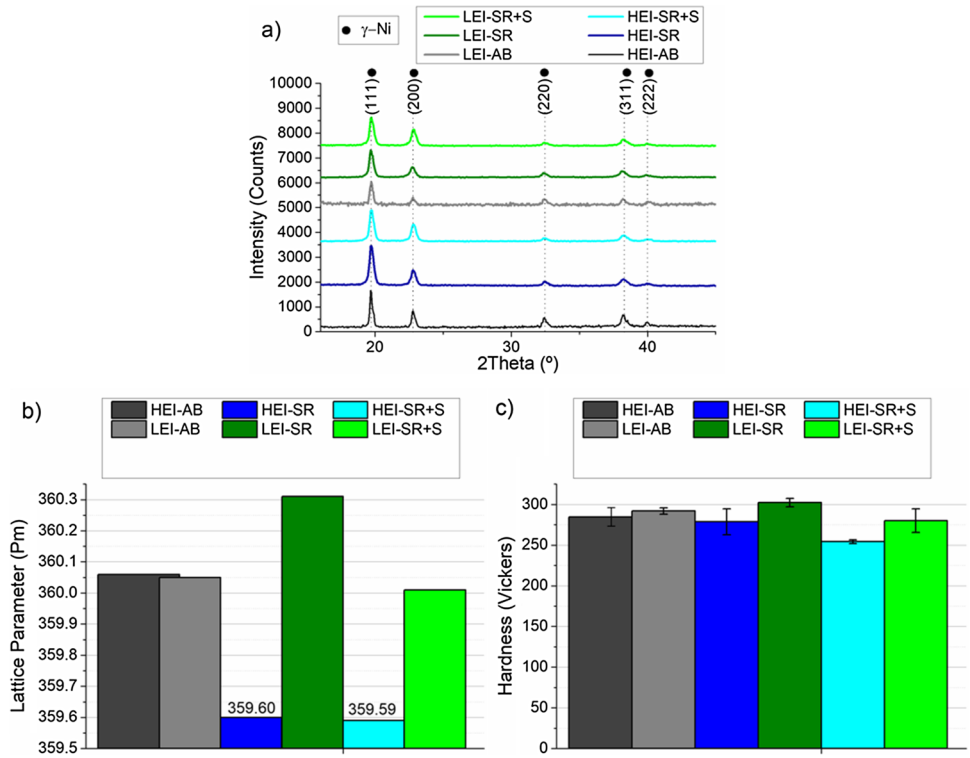

Fig. 6 X-ray diffraction patterns, **b**) lattice parameter, and **c** hardness of the as-built and heat-treated samples of IN625. Only γ-Ni phase FCC peaks are observed

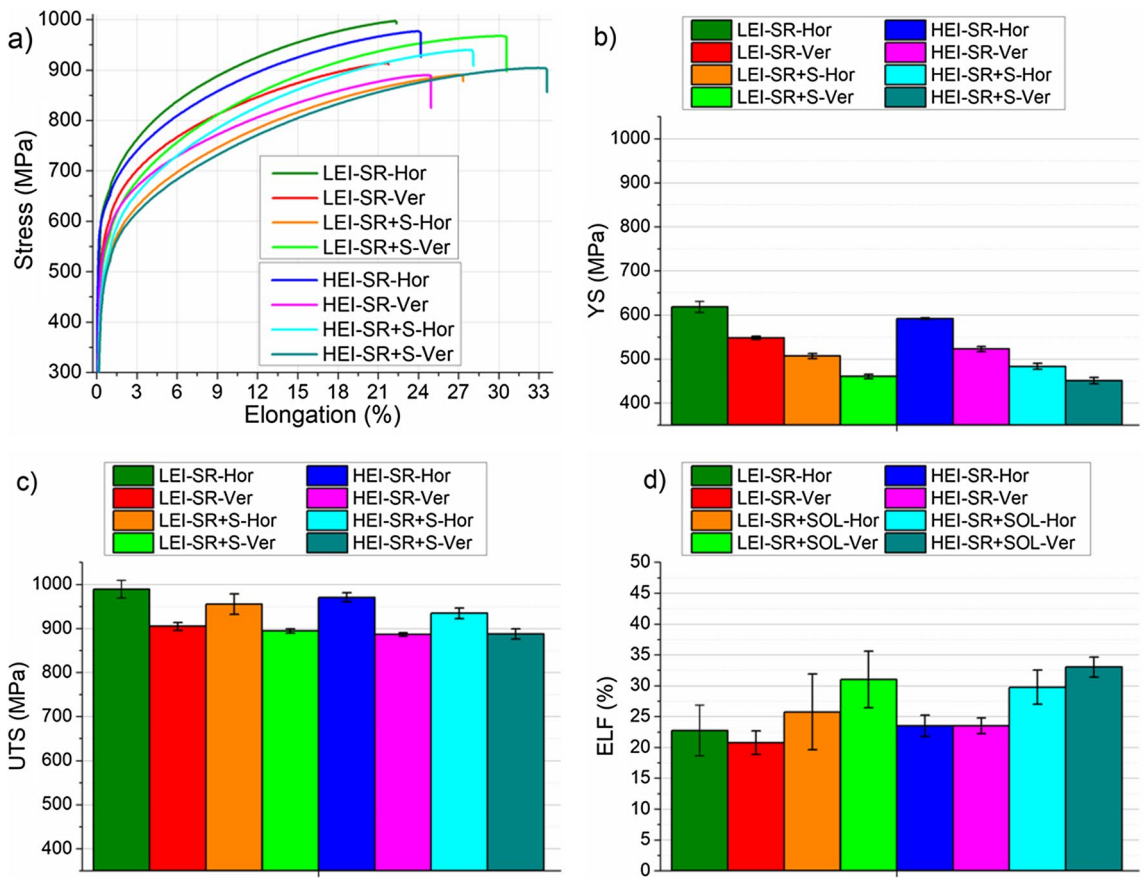

Fig. 7 Tensile test results for heat-treated samples built in the vertical and horizontal direction showing **a** typical tensile-elongation engineering curves, **b** yield strength (YS), **c** ultimate tensile strength (UTS), and **d** elongation to fracture (ELF). The tests were conducted at room temperature

vertical building direction orientation when compared with the horizontal one. The UTS is similar to LEI and HEI. However, the UTS of vertical samples is always lower than horizontal samples. The ELF shows an increase with solubilization heat treatment, and a slightly higher elongation was observed for the HEI condition. Notice that ELF is not affected by the SR heat treatment, but its values are higher in the vertical direction than in the horizontal direction.

3.3 Impact testing results

Figure 8 summarizes the impact energy test results of the heat-treated samples. From Fig. 8a, the impact toughness increases with solubilization heat treatment for both LEI and HEI conditions. The average impact toughness of HEI – SR is slightly higher than LEI – SR and continues to be higher with applied solubilization heat treatment for both conditions. Figure 8 b–e show the SEM images of the resulting fracture surfaces after the impact tests, where Fig. 8b–c show the HEI – SR + S and Fig. 8d–e show the LEI – SR + S. The columnar direction of the structure is indicated in Fig. 8b with the dashed red line. At the same time, an undissolved particle is highlighted with a yellow dashed line and magnified in Fig. 8c. As noted, fracture surfaces mostly comprise dimples, indicating ductile behavior, corroborating with high ELF results found on tensile tests, as shown in a dimple in Fig. 8d. Figure 8 e shows a secondary crack propagating in a different direction from the main crack; however, dimples are also evidenced. This ductile behavior was similar for the fracture surfaces in the other conditions.

4 Discussion

4.1 Macrofeatures and microfeatures

In this study, the LDED process successfully manufactured Inconel 625 samples under two different manufacturing regimes, and two heat treatments were analyzed and compared between them and the as-built condition. As shown in Table 2, despite heat source power levels being somewhat similar, the energy density, efficiency, and layer height are distinct, with the HEI condition being 57% higher than the LEI condition. Such differences can be attributed to the transverse speed at which each condition was built. Higher transverse speeds allow a shorter deposition time in one spot, decreasing the built's height compared to low

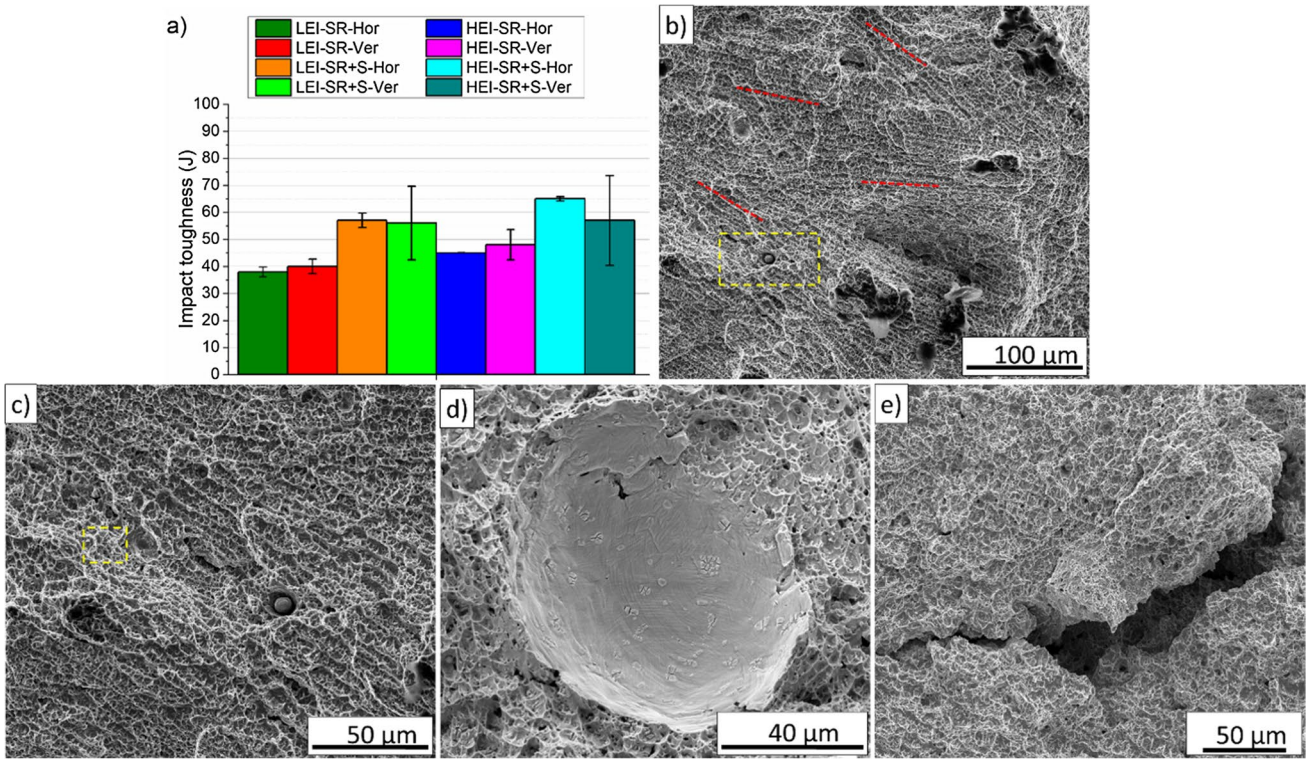

Fig. 8 Impact energy results of heat-treated conditions showing **a** impact energy values and SEM images of fracture surfaces after impact tests of the HEI (**b**–**c**) and LEI (**d**–**e**) after SR + S. Dashed red lines in **b** indicate that the columnar structure parallels crack growth propagation. **c** Detail of unmelted particles and dimple-like structures; **d** detail of cavities and **e** dimple-like structures. The undissolved particle is highlighted with a yellow dashed line

transverse speeds. The macros show that lower transverse speeds (HEI) lead to higher layers.

According to XRD results, it was not observed the expected intermetallic phases calculated under equilibrium: NbC, σ, and Ni_3Nb, probably due to their small size and volume fraction [7]. It is worth mentioning that precipitates were not observed even at the log scale. Dinda et al. [11] mentioned that γ' [Ni_3Al], γ'' [Ni_3Nb], and δ [Ni_3Nb] may precipitate in the γ-Ni matrix. However, there is no Al in the alloy composition. γ'' and δ phases were differentiated by Dinda et al. [11] by the type of interface with matrix, where γ'' precipitates coherent and δ incoherent. The authors tracked the presence of those precipitates using the change in lattice parameter of the γ-Ni phase.

Although the γ-Ni lattice parameter has similar values in the as-built condition for HEI and LEI samples, the heat treatments were affected differently in both processing conditions. With the SR cycle, the γ-Ni lattice parameter decreases for the HEI condition, while the opposite occurs for the LEI condition. The rejection of elements from the matrix can explain the reason for the decrease. Rejected Nb forms Ni_3Nb, which comprises 6.5 vol. % at 800 °C under equilibrium conditions, while rejected Mo forms the Mo-rich σ phase, which shall consist of 9.2 vol. % when calculated at the same temperature. Rodrigues et al. [22] observed similar behavior with synchrotron XRD for heat treatment at 870 °C for 1 h. On the other hand, the increase in lattice parameters can be attributed to the dissolution of precipitates in the matrix.

Despite both heat treatments being successful regarding their mechanical behavior in hardness, tensile, and toughness tests, a deeper and thorough analysis of its microstructure and lattice parameters showed some details that should be considered. Figure 6 shows that the HEI condition, in both heat treatments, has a smaller lattice parameter value than the LEI condition. Usually, smaller lattice parameter values, when compared among different states, can be attributed to the presence/formation of precipitates, intermetallic particles, or carbides, for example, since the precipitation of particles can affect the rearrangement of the atoms in the lattice, causing small deformations and micro-stresses, which alter the lattice spacing [7]. What is particularly intriguing in this case is that when comparing LEI and HEI conditions, it seems that precipitates or intermetallic particles stayed in the HEI sample microstructure despite undergoing high-temperature heat treatments and even solubilization. One possible explanation for this is that some superalloys with thermal history, due to the high temperature of the heat treatments, can reach high enough temperatures, which contributes to raising concentrations of elements like Nb, Mo, and Cr high sufficiently so they can precipitate in a rapid enough eutectic reaction, mostly in interdendritic spaces [26, 27]. Moreover, it is possible to notice that the microstructure is shifting from dendritic structures to a more granular structure, as seen in Fig. 3a–f. The grain structure is not fully developed, as shown in Fig. 3e–f, which can be associated with insufficient time or temperature during the solubilization treatment [7, 25].

Regarding the stronger texture developed in HEI samples, it shows little influence on mechanical properties (Figs. 5, 7 and 8). The main difference can be observed for elongation and impact toughness, which is higher for HEI conditions. YS shows to be slightly lower for HEI samples, suggesting that the texture developed affects it in an undesired way. The mechanical strength parameters can also be correlated with the microstructure quality after processing, and these parameters may vary by two major factors: process parameters and heat treatments. For example, the resulting microstructure in AM processes varies with the heat source power of the laser, feed rate, layer thickness, and deposition rate. Although, in this case, the HEI condition presented lower hardness values and lower mechanical strength, with a higher ELF when compared to the LEI condition, this difference also depends on an effect of finer layers, consequently, more refined microstructure and distribution of brittle phase. The σ phase, which will be further detailed, is an inherent phase of the solidification process of as-deposited Inconel 625, located in the inter-dendritic regions, implying higher hardness and brittleness. These properties result in stress concentration points, nucleating and propagating cracks during sample traction, decreasing the material's ductility [8]. Horizontal samples presented a higher mechanical response than the vertical building direction.

Figure 9 shows microstructure feature details for some conditions. It can be noticed that the microstructure has particles scattered throughout the matrix. Moreover, liquation cracks were found for both conditions, mostly in the HEI condition, as shown with the blue arrow in Fig. 9d and e. This could be due to each condition's thermal input during the process, as the HEI condition has a larger heat input when compared to the LEI condition, which occurs due to half the transverse speed with a similar deposition rate, as seen in Table 2 [28]. Furthermore, alloys with larger differences between solidus and liquidus temperatures, such as Ni-based superalloys, are susceptible to this type of cracking, in which some grain boundary precipitates melt during the rapid heating and the evolution of stresses due to solidification and thermal contractions during cooling [3].

Particles inside the grains, shown in Fig. 9, could have precipitated during the cooling process in Nb and Mo-rich regions, mostly grain boundaries and inter-dendritic spaces. Upon EDS analysis of the particles, shown in Fig. 9g and h, it is possible to notice similarities with Laves phase precipitates when comparing results with the literature [21]. As shown by the blue arrows in Fig. 9a–b and d–e, the HEI condition and liquation cracks seem to have more σ phase

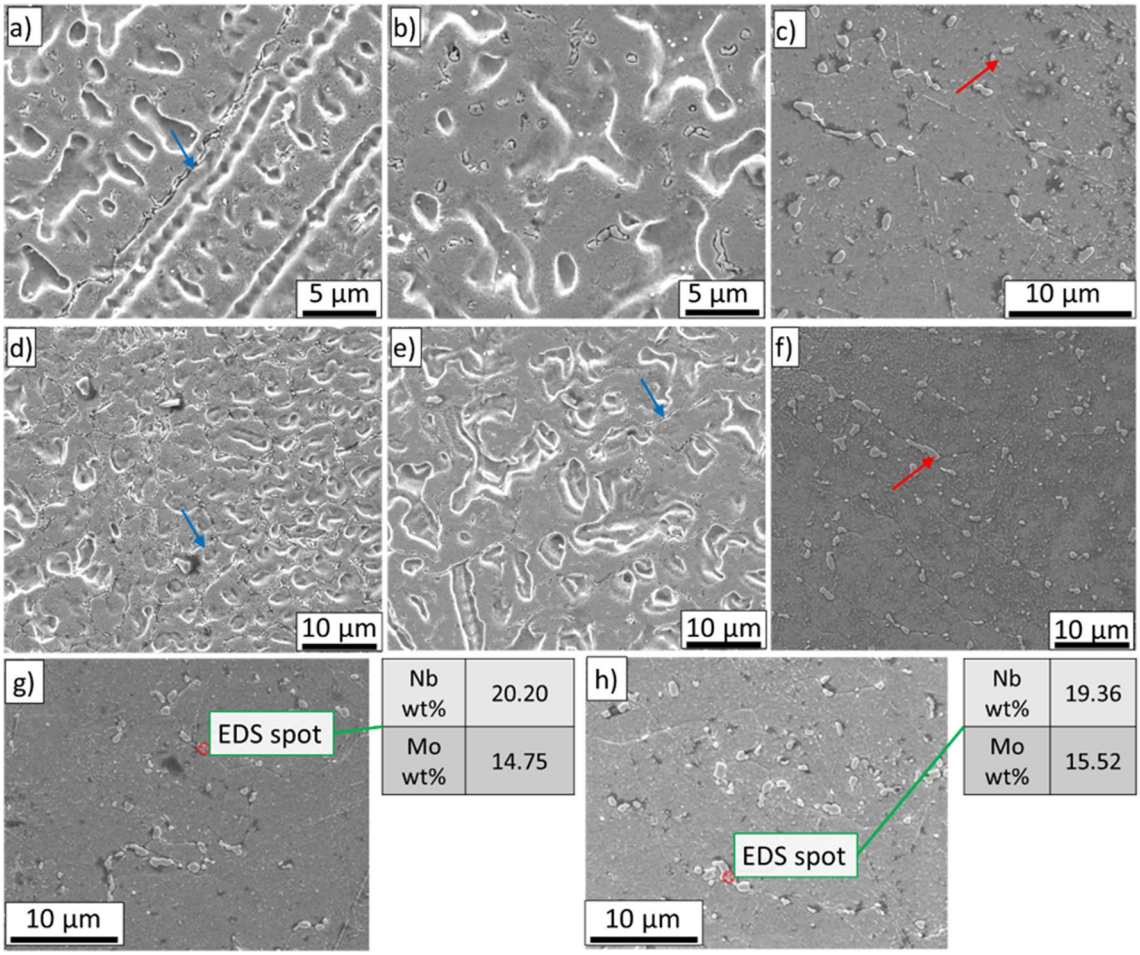

Fig. 9 Microstructural features details for LEI (first row) and HEI (second row) conditions, showing **a**, **d** as built, **b**, **e** after stress relief heat treatment, and **c**, **f** after the combination of stress relief and solubilization heat treatment. EDS of the σ phases at the stress relief + solution heat treatment: **g** LEI and **h** HEI

in the solution condition than the LEI. It can be noticed that σ phase particles are presented here in two forms: coarse, dispersed, and worm-like along liquefaction cracks.

4.2 Mechanical properties

As shown in Fig. 10, samples that go through solubilization treatments tend to present a higher ELF with lower UTS than non-solubilized samples [23]. Another feature observed is that ductile materials will often absorb more energy on impact [29], which also happened and can be noticed in Fig. 8. Likewise, the same conclusion pops out when comparing the results presented in Figs. 6 and 7. In addition, horizontal samples showed a higher mechanical strength with little effect on the ELF, also reported in previous work [23].

Nevertheless, the mechanical strength follows the decreasing trend with an ELF increase of former results. We did not find ELF values higher than 33%, while other authors reported values higher than 43% for LDED and 56% for LPBF [7]. Still, the mechanical response after the heat treatment depends on the AM processing parameters regarding heat source power, transverse speed, and layer height. Since mechanical properties are similar between conditions, we did not notice any deleterious effect of the lower density in the LEI condition regarding the HEI condition.

Puppala et al. [29] reported that the as-built condition presented values of 46.5–48.5 J and 51.7 J after a stress-relief heat treatment at 950 °C/1 h. This study conducted stress relief at a lower temperature, and mechanical properties did not change as much compared to the as-built condition. Therefore, the results are close to the values presented by Puppala et al. In contrast, solubilization in this work was conducted at a higher temperature, increasing the impact energy to values above 55 J, even higher than the reported in the former work. In addition, the impact toughness is higher in the HEI condition, i.e., a state that presented less hardness and higher elongation to fracture. Hence, the effect of the building orientation is unclear for impact properties.

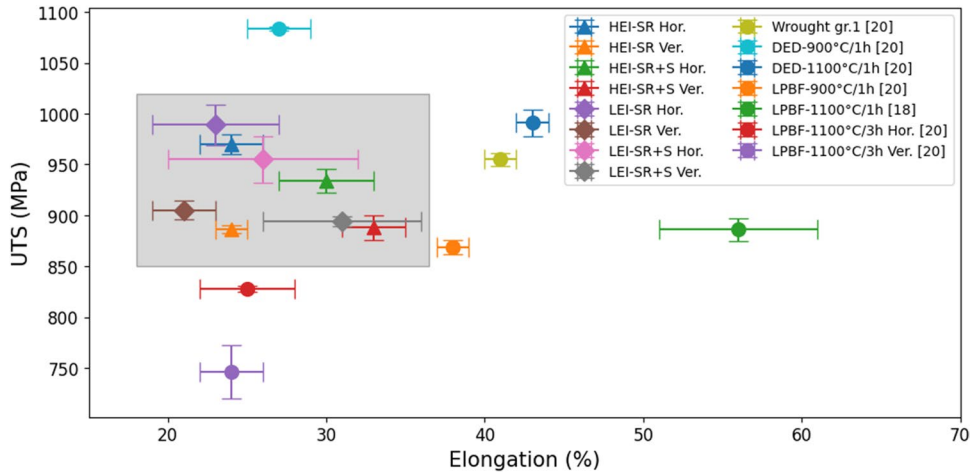

Fig. 10 Mechanical properties comparison. The squared area highlights the properties found in the present work

5 Conclusions

- The HEI condition delivers parts with a layer height of 63% higher, with more efficiency and less energy density than the LEI condition. Therefore, the HEI condition offers attractive processing conditions without reducing mechanical strength.
- Although the LEI condition presented a slight porosity density than the HEI condition, there was also a slight increase in mechanical properties. Therefore, the low porosity of the samples did not affect the mechanical properties. The HEI and LEI condition differences are not statistically significant. Hence, the horizontal direction depicted a better mechanical behavior. The differences between horizontal and vertical building directions, as observed in the tensile and Charpy results, depict the effect of anisotropy due to the process parameters.
- The stress relief at 800 ºC for 1 h improves the yield strength and reduces the elongation to fracture, while the stress relief + solution (1100 ºC for 1 h) reduces the yield strength and increases the elongation to fracture. However, no statistical changes were found in the ultimate tensile strength. Therefore, long solution treatments larger than 3 h will be needed to recrystallize the columnar microstructure completely.

Funding Open Access funding provided thanks to the CRUE-CSIC agreement with Springer Nature. This study was financed by The Sao Paulo Research Foundation (FAPESP), grant No. 20/09079–2. This study was financed in part by the Coordenação de Aperfeiçoamento de Pessoal de Nível Superior – Brasil (CAPES) –Finance Code 001 and the Conselho Nacional de Desenvolvimento Científico e Tecnológico (CNPq) under grants 306960/2021–4 and 350883/2023-8. Julian A. Avila is a Serra Húnter Fellow.

Data availability The data supporting this study's findings are available from the corresponding author, J. A. Avila, upon reasonable request.

Declarations

Competing interests The authors declare no competing interests.

Open Access This article is licensed under a Creative Commons Attribution 4.0 International License, which permits use, sharing, adaptation, distribution and reproduction in any medium or format, as long as you give appropriate credit to the original author(s) and the source, provide a link to the Creative Commons licence, and indicate if changes were made. The images or other third party material in this article are included in the article's Creative Commons licence, unless indicated otherwise in a credit line to the material. If material is not included in the article's Creative Commons licence and your intended use is not permitted by statutory regulation or exceeds the permitted use, you will need to obtain permission directly from the copyright holder. To view a copy of this licence, visit http://creativecommons.org/licenses/by/4.0/.

References

1. Dutta B, Babu S, Jared B (2019) Science, technology and applications of metals in additive manufacturing. Elsevier. https://doi.org/10.1016/C2017-0-04707-9
2. Jiang M, Mukherjee T, Du Y, DebRoy T (2022) Superior printed parts using history and augmented machine learning. NPJ Comput Mater 8(1):184. https://doi.org/10.1038/s41524-022-00866-9
3. Svetlizky D, Das M, Zheng B, Vyatskikh AL, Bose S, Bandyopadhyay A, Schoenung JM, Lavernia EJ, Eliaz N (2021) Directed energy deposition (DED) additive manufacturing: physical characteristics, defects, challenges and applications. Mater Today 49:271–295. https://doi.org/10.1016/j.mattod.2021.03.020
4. Gradl PR, Protz C, Wammen T (2019) Additive manufacturing development and hot-fire testing directed energy deposition Inconel 625 and JBK-75 alloys. 55th AIAA/SAE/ASEE J Propulsion Conf 2019:1–20
5. Shankar V, BhanuSankara Rao K, Mannan SL (2001) Microstructure and mechanical properties of Inconel 625 superalloy. Journal of Nuclear Materials [Internet] 288:222–232 (https://linkinghub.elsevier.com/retrieve/pii/S0022311500007236)
6. Fullen MD, Schneider JA (2019) Effects of varying heat treatments on the microstructure and mechanical properties of blown

powder Inconel 625. Jom [Internet]. 71:1127–1133. https://doi.org/10.1007/s11837-019-03339-5
7. Nguejio J, Szmytka F, Hallais S et al (2019) Comparison of microstructure features and mechanical properties for additive manufactured and wrought nickel alloys 625. Mater Sci Eng, A 764:138214
8. Hu Y, Lin X, Li Y et al (2021) Microstructural evolution and anisotropic mechanical properties of Inconel 625 superalloy fabricated by directed energy deposition. J Alloys Compd [Internet]. 870:159426 (https://linkinghub.elsevier.com/retrieve/pii/S0925838821008355)
9. Kreitcberg A, Brailovski V, Turenne S (2017) Effect of heat treatment and hot isostatic pressing on the microstructure and mechanical properties of Inconel 625 alloy processed by laser powder bed fusion. Materials Science and Engineering A [Internet]. 689:1–10. https://doi.org/10.1016/j.msea.2017.02.038
10. Chen S, Gao H, Zhang Y et al (2022) Review on residual stresses in metal additive manufacturing: formation mechanisms, parameter dependencies, prediction and control approaches. J Market Res 17:2950–2974
11. Chandler H (ed) (1996) Heat treater's guide: practices and procedures for nonferrous alloys. ASM international, p 657
12. Stoudt MR, Lass EA, Ng DS et al (2018) The influence of annealing temperature and time on the formation of δ-phase in additively-manufactured Inconel 625. Metall Mater Trans A Phys Metall Mater Sci 49:3028–3037
13. Lass EA, Stoudt MR, Williams ME et al (2017) Formation of the Ni3Nb δ-phase in stress-relieved Inconel 625 produced via laser powder-bed fusion additive manufacturing. Metall Mater Trans A Phys Metall Mater Sci 48:5547–5558
14. Fullen MD, Schneider JA (2019) Effects of varying heat treatments on the microstructure and mechanical properties of blown powder Inconel 625. Jom 71:1127–1133
15. Farias FWC, Duarte VR, Felice IO et al (2023) In situ interlayer hot forging arc-based directed energy deposition of Inconel® 625: process development and microstructure effects. Addit Manuf [Internet]. 66:103476 (https://linkinghub.elsevier.com/retrieve/pii/S2214860423000891)
16. ASTM F3056 (2021) Standard specification for additive manufacturing nickel alloy (UNS N06625) with powder bed fusion. ASTM International, West Conshohocken, PA. https://doi.org/10.1520/F3056-14
17. Thiesen Junior A (2021) Selection of processing parameters for the laser directed energy deposition process applied to additive manufacturing: a methodological proposal. Dissertation thesis, Federal University of Santa Catarina. https://repositorio.ufsc.br/handle/123456789/227036. Accessed 11 Mar 2022
18. ASTM E8/E8M (2016) Standard test methods for tension testing of metallic materials. ASTM International, West Conshohocken, PA. https://doi.org/10.1520/E0008_E0008M-16AE01
19. ASTM E23 (2003) Standard test methods for notched bar impact testing of metallic materials. ASTM International, West Conshohocken, PA. https://doi.org/10.1520/E0023-12C.2
20. Vander Voort G, Manilova E (2004) Metallographic techniques for superalloys. Microscopy and Microanalysis [Internet]. 10:690–691 (https://academic.oup.com/mam/article/10/S02/690/6913058)
21. Kong Y, Huang H (2022) Effect of intrinsic heat treatment on microstructure and hardness of additively manufactured Inconel 625 alloy by directed energy deposition. Mater Des [Internet]. 224:111279 (https://linkinghub.elsevier.com/retrieve/pii/S0264127522009017)
22. Rodrigues TA, Cipriano Farias FW, Avila JA, et al (2023) Effect of heat treatments on Inconel 625 fabricated by wire and arc additive manufacturing: an in situ synchrotron X-ray diffraction analysis. Science and Technology of Welding and Joining [Internet].1–6. https://www.tandfonline.com/doi/full/10.1080/13621718.2023.2187927.
23. De Terris T, Castelnau O, Hadjem-Hamouche Z et al (2021) Analysis of as-built microstructures and recrystallization phenomena on Inconel 625 alloy obtained via laser powder bed fusion (L-PBF). Metals (Basel) [Internet] 11:619
24. Marchese G, Parizia S, Rashidi M et al (2020) The role of texturing and microstructure evolution on the tensile behavior of heat-treated Inconel 625 produced via laser powder bed fusion. Materials Science and Engineering: A [Internet]. 769:138500 (https://linkinghub.elsevier.com/retrieve/pii/S0921509319312869)
25. Dinda GP, Dasgupta AK, Mazumder J (2009) Laser aided direct metal deposition of Inconel 625 superalloy: microstructural evolution and thermal stability. Materials Science and Engineering: A [Internet]. 509:98–104 (https://linkinghub.elsevier.com/retrieve/pii/S0921509309000215)
26. Antonsson T, Fredriksson H (2005) The effect of cooling rate on the solidification of INCONEL 718. Metallurgical Mater Trans B [Internet]. 36:85–96. https://doi.org/10.1007/s11663-005-0009-0
27. Chlebus E, Gruber K, Kuźnicka B et al (2015) Effect of heat treatment on the microstructure and mechanical properties of Inconel 718 processed by selective laser melting. Materials Science and Engineering: A [Internet]. 639:647–655 (https://linkinghub.elsevier.com/retrieve/pii/S0921509315005687)
28. Kou S (2003) Solidification and liquation cracking issues in welding. JOM [Internet]. 55:37–42 (https://link.springer.com/10.1007/s11837-003-0137-4)
29. Puppala G, Moitra A, Sathyanarayanan S et al (2014) Evaluation of fracture toughness and impact toughness of laser rapid manufactured Inconel-625 structures and their co-relation. Mater Des [Internet]. 59:509–515. https://doi.org/10.1016/j.matdes.2014.03.013

Publisher's Note Springer Nature remains neutral with regard to jurisdictional claims in published maps and institutional affiliations.